Biometrics VV, 1–19 DOI: DOI HERE
Month YYYY

A Bayesian Model to Enhance Complex-Valued Measurements Applied to Functional Magnetic Resonance Imaging

John Bodenschatz*, and Daniel Rowe**

Department of Mathematical and Statistical Sciences, Marquette University, Milwaukee, WI, U.S.A.

**email:* john.bodenschatz@marquette.edu

***email:* daniel.rowe@marquette.edu

Summary: Many real-world applications in digital signal processing demand the use of mathematical and statistical methods that support complex-valued data. We examine the case of signal degradation over time, in particular, as it applies to functional magnetic resonance imaging (fMRI). This attenuated signal can be amplified through a variety of methods. We outline a formal Bayesian approach to enhance the noisy signal, increasing the signal-to-noise ratio. We will demonstrate that the first three images in an fMRI time series can be used to enhance the remaining images, improving the signal-to-noise ratio and contrast within these images. The model preserves the ability to detect complex-valued task-related blood oxygenation level dependent (BOLD) signal increases. This model was evaluated through simulated data and applied to right-hand finger tapping experimental fMRI data.

Key words: Bayesian; Complex-Valued; FMRI; K-space.

1. Introduction

Many real-world applications, in particular digital signal processes, require the support for complex-valued data. It is also a common problem in digital signal applications to have a loss or degradation of signal quality over time as a result of various factors. One real-world application that experiences both of these challenges is functional magnetic resonance imaging (fMRI). FMRI experiments are non-invasive procedures that involve a patient performing some task or observing some stimulus. There is a blood oxygenation level dependent (BOLD) signal increase in the region of the brain associated with this task (Ogawa et al., 1990). The BOLD response is considered to be a correlate of neuronal response to the task or stimulus (Harris et al., 2011; Mullinger et al., 2014; Shmuel and Leopold, 2008). Images collected while the patient is at rest are compared to images collected while the patient is performing the task or observing the stimulus. The slight difference in the images is analyzed, resulting in detection of the BOLD signal change.

In fMRI, complex-valued spatial frequency coefficients in k-space are measured over time. Initially these frequency coefficients have a very strong signal. However, due to physical properties of the bodily tissues (in particular, T_1 relaxation times) and the operation of the machine, the signal quality quickly degrades to a steady state at a much lower strength than the initial measurements. These k-space arrays are inverse Fourier reconstructed into complex-valued images, where the signal degradation among the first four images is made more clear. All remaining images in the time series after the first two or three are of significantly lesser quality which increases the difficulty of making qualitative and quantitative observations. This will be further explored in Section 4.

We choose to employ a Bayesian model to address this problem. The Bayesian approach provides three main advantages: minimal computational expense, interpretable procedures, and results. We will show that *a priori* data that is of higher quality than the remaining measured data can be used to assess hyperparameters of known distributions that can be joined with the observed (likelihood) data and used to form *a posteriori* estimates of the data. This posterior estimated data will have increased signal magnitude and decreased noise, resulting in a significantly greater signal-to-noise ratio (SNR). Resulting data will have improved fidelity, a more accurate representation of the true object being imaged, which enhances the ability to draw conclusions and make determinations about the data.

2. Bayesian Approach

2.1 *Likelihoods*

As has been demonstrated, the real and imaginary parts of the measured complex-valued signal, x_R and x_I, are independent and identically normally distributed (den Dekker and Sijbers, 2005; Gudbjartsson and Patz, 1995; Rowe, 2023). The means are given by $\mu_R = \rho\cos(\theta)$ and $\mu_I = \rho\sin(\theta)$ with a common variance σ^2, where ρ is the true signal magnitude and θ is the true signal phase. The joint distribution of the real and imaginary components is given by

$$f(x_R, x_I|\rho,\theta,\sigma^2) = \frac{1}{(2\pi\sigma^2)^{1/2}}\exp\left[-\frac{(x_R-\rho\cos(\theta))^2}{2\sigma^2}\right] \times \frac{1}{(2\pi\sigma^2)^{1/2}}\exp\left[-\frac{(x_I-\rho\sin(\theta))^2}{2\sigma^2}\right]. \quad (1)$$

A transformation of variables from Cartesian to polar coordinates $(x_R, x_I) \rightarrow (r,\phi)$ using $x_R = r\cos(\phi)$ and $x_I = r\sin(\phi)$, on Equation 1 is performed. The Jacobian $J = r$ is calculated, and we arrive at the joint distribution

$$f(r,\phi|\rho,\theta,\sigma^2) = \frac{r}{2\pi\sigma^2}\exp\left[-\frac{1}{2\sigma^2}\left[r^2+\rho^2-2r\rho\cos(\phi-\theta)\right]\right]. \quad (2)$$

We can integrate out the measured phase ϕ from Equation 2 to arrive at the Ricean marginal distribution of the measured magnitude r (Rice, 1944)

$$f(r|\rho,\sigma^2) = \frac{r}{\sigma^2}\exp\left[-\frac{r^2+\rho^2}{2\sigma^2}\right] I_0\left(\frac{r\rho}{\sigma^2}\right). \quad (3)$$

Here I_0 is the zeroth order modified Bessel function of the first kind. The mean of this Ricean distribution is $\sigma\sqrt{\pi/2}L_{1/2}(-\rho^2/2\sigma^2)$ and the variance is given by $2\sigma^2+\rho^2-\frac{\pi\sigma^2}{2}L_{1/2}^2(-\rho^2/2\sigma^2)$, where $L_{1/2}$ is a Laguerre polynomial. If the true signal ρ is small, $\rho \approx 0$, Equation 3 becomes the Rayleigh distribution with mean $\sigma\sqrt{\frac{\pi}{2}}$ and variance $\frac{4-\pi}{2}\sigma^2$ (Rayleigh, 1880). If the true signal ρ is high, this becomes the normal distribution with mean ρ and variance σ^2. Integrating out the measured magnitude r from the joint distribution in Equation 2 gives an unnamed non-normal distribution marginal distribution of the measured phase ϕ,

$$f(\phi|\rho,\theta,\sigma^2)=\frac{1}{2\pi}\exp\left[-\frac{\rho^2}{2\sigma^2}\right]\times\left[1+\frac{\rho}{\sigma}\sqrt{2\pi}\cos(\phi-\theta)\exp\left[\frac{\rho^2\cos^2(\phi-\theta)}{2\sigma^2}\right]\Phi\left(\frac{\rho\cos(\phi-\theta)}{\sigma}\right)\right], \tag{4}$$

where $\Phi(x)$ is the cumulative distribution function of the standard normal distribution (Lathi, 1983; Rowe and Bodenschatz, 2025). When the true signal ρ is near zero, the measured phase will be uniformly distributed on $[-\pi,\pi]$ with mean 0 and variance $\frac{\pi^2}{3}$. When the true signal ρ becomes large, the distribution of the measured phase becomes normal with mean θ and variance $\frac{\sigma^2}{\rho^2}$. It is between these zero and high SNR scenarios that we are concerned with.

The joint distribution for the measured magnitude and phase as in Equation 2 can be expressed as the product of the marginal distribution of the magnitude and the conditional distribution of the phase given the magnitude r,

$$f(r,\phi|\rho,\theta,\sigma^2)=f(r|\rho,\sigma^2)f(\phi|r,\rho,\theta,\sigma^2). \tag{5}$$

Dividing the joint distribution $f(r,\phi)$ in Equation 2 by the marginal distribution for ϕ in Equation 4, we see that the conditional distribution of the phase ϕ given magnitude r is von Mises (Von Mises, 1918)

$$f(\phi|r,\rho,\theta,\sigma^2)=\frac{\exp\left[\frac{r\rho\cos(\phi-\theta)}{\sigma^2}\right]}{2\pi I_0\left(\frac{r\rho}{\sigma^2}\right)}. \tag{6}$$

This von Mises distribution has mean θ and variance $1-\frac{I_1(r\rho/\sigma^2)}{I_0(r\rho/\sigma^2)}$. In summary, the likelihoods for the measured data are $r\sim Rice(\rho,\sigma)$ and $\phi|r\sim VM(\theta,\frac{r\rho}{\sigma^2})$.

2.2 *Priors*

Using the same family of distributions, we select the priors to be conjugate to the likelihoods for a simpler estimation of the parameters and because of well-known data distributions. The prior distribution of the true magnitude ρ is Ricean,

$$f(\rho|\rho_0,\sigma^2,\gamma)=\frac{\rho}{\sigma^2/\gamma}\exp\left[-\frac{\rho^2+\rho_0^2}{2\sigma^2/\gamma}\right]I_0\left(\frac{\rho\rho_0}{\sigma^2/\gamma}\right), \tag{7}$$

with hyperparameters ρ_0 and γ. Similarly to the marginal distribution for the measured magnitude r as in Equation 3, the distribution in Equation 7 becomes the Rayleigh distribution when $\rho_0 \sim 0$ and the normal distribution when ρ_0 is large. The prior distribution of the true phase θ given the magnitude is von Mises,

$$f(\theta|\rho, \sigma^2, \theta_0, \gamma) = \frac{\exp\left[\frac{\rho\rho_0 \cos(\theta-\theta_0)}{\sigma^2/\gamma}\right]}{2\pi I_0\left(\frac{\rho\rho_0}{\sigma^2/\gamma}\right)}, \tag{8}$$

with location hyperparameter θ_0. The von Mises distribution in Equation 8 becomes the uniform distribution on $[-\pi, \pi]$ when $\rho_0 \sim 0$ and the normal distribution when ρ_0 is large. Both the Ricean distribution in Equation 7 and the von Mises distribution in Equation 8 become vague with a small γ. Lastly, we assess a prior for the variance σ^2 with an inverse gamma distribution

$$f(\sigma^2|\alpha, \beta) = \frac{\beta^\alpha}{\Gamma(\alpha)(\sigma^2)^{\alpha+1}} \exp\left[-\frac{\beta}{\sigma^2}\right], \tag{9}$$

with hyperparameters of shape α and scale β. The inverse gamma distribution becomes vague when α and β are small. In summary, the prior distributions are $\rho|\sigma \sim Rice(\rho_0, \sigma/\sqrt{\gamma})$, $\theta|\rho, \sigma \sim VM(\theta_0, \frac{\rho\rho_0}{\sigma^2/\gamma})$, and $\sigma \sim IG(\alpha, \beta)$.

2.3 *Posteriors*

The likelihoods from Equations 3 and 6 can be combined with the priors in Equations 7-9 to obtain the posterior distribution

$$f(\rho, \theta, \sigma^2|r, \phi) \propto f(r|\rho, \sigma^2) f(\phi|r, \rho, \theta, \sigma^2) \times f(\rho|\sigma^2, \gamma) f(\theta|\rho, \sigma^2, \theta_0, \gamma) f(\sigma^2|\alpha, \beta), \tag{10}$$

or,

$$\begin{aligned} f(\rho, \theta, \sigma^2|r, \phi) \propto{}& \frac{r}{\sigma^2} \exp\left[-\frac{r^2+\rho^2}{2\sigma^2}\right] I_0\left(\frac{r\rho}{\sigma^2}\right) \frac{\exp\left[\frac{r\rho\cos(\phi-\theta)}{\sigma^2}\right]}{2\pi I_0\left(\frac{r\rho}{\sigma^2}\right)} \\ &\times \frac{\rho}{\sigma^2} \exp\left[-\frac{\rho^2+\rho_0^2}{2\sigma^2/\gamma}\right] I_0\left(\frac{\rho\rho_0}{\sigma^2/\gamma}\right) \frac{\exp\left[\frac{\rho\rho_0\cos(\theta-\theta_0)}{\sigma^2/\gamma}\right]}{2\pi I_0\left(\frac{\rho\rho_0}{\sigma^2/\gamma}\right)} \times \frac{\beta^\alpha}{\Gamma(\alpha)(\sigma^2)^{\alpha+1}} \exp\left[-\frac{\beta}{\sigma^2}\right]. \end{aligned} \tag{11}$$

Some simplification leads to the joint posterior distribution

$$\begin{aligned} f(\rho, \theta, \sigma^2|r, \phi) \propto{}& \frac{\beta^\alpha}{\Gamma(\alpha)} \exp\left[-\frac{1}{2\sigma^2}\left(\gamma\rho_0^2 + r^2 + 2\beta\right)\right] \frac{\rho}{(\sigma^2)^{\alpha+3}} \\ &\times \exp\left[-\frac{1}{2\sigma^2}\left((\gamma+1)\rho^2 - 2\rho(\rho_0\cos(\theta-\theta_0) + r\cos(\phi-\theta))\right)\right]. \end{aligned} \tag{12}$$

The posterior conditional distributions can be found by considering only the terms that contain the parameter of interest. The posterior conditional distribution of the magnitude ρ given the phase θ and variance σ^2 can be shown to be Modified-Half-Normal (MHN) distributed (Sun et al., 2023)

$$f(\rho|\theta,\sigma^2,r,\phi) = \frac{2B^{A/2}\rho^{A-1}}{\Psi\left(\frac{A}{2},\frac{C}{\sqrt{B}}\right)} \exp\left[-B\rho^2 + C\rho\right], \tag{13}$$

where Ψ is the Fox-Wright Psi function (Fox, 1928; Wright, 1935), $A = 2$, $B = (\gamma+1)/(2\sigma^2)$, and $C = \left[\rho_0\gamma\cos(\theta-\theta_0) + r\cos(\phi-\theta)\right]/\sigma^2$. The MHN is a relatively new distribution with no known applications at the time of this writing. Further, it can be shown that the posterior conditional distribution of the phase θ given the magnitude ρ and variance σ^2 is von Mises

$$f(\theta|\rho,\sigma^2,r,\phi) = \frac{\exp\left[\kappa\cos(\theta-\lambda)\right]}{2\pi I_0\left(\kappa\right)}, \tag{14}$$

where $\kappa = c\rho/\sigma^2$, $a = \rho_0\gamma\cos(\theta_0) + r\cos(\phi)$, $b = \rho_0\gamma\sin(\theta_0) + r\sin(\phi)$, $c = \text{sign}(a)\sqrt{a^2+b^2}$, and $\lambda = \arctan(b/a)$. Lastly, the posterior distribution of the variance σ^2 given the magnitude ρ and phase θ is an inverse gamma distribution

$$f(\sigma^2|\rho,\theta,r,\phi) = \frac{(\beta_*)^{\alpha_*}}{\Gamma(\alpha_*)(\sigma^2)^{\alpha_*+1}} \exp\left[-\frac{\beta_*}{\sigma^2}\right], \tag{15}$$

where $\beta_* = \left[(\gamma+1)\rho^2 - 2\rho(\rho_0\gamma\cos(\theta-\theta_0) + r\cos(\phi-\theta)) + (\gamma\rho_0^2 + r^2 + 2\beta)\right]/2$ and $\alpha_* = \alpha + 2$. In summary, the posterior conditional distributions are $\rho|\theta,\sigma^2 \sim MHN(A,B,C)$, $\theta|\rho,\sigma^2 \sim VM(\lambda,\kappa)$, and $\sigma^2|\rho,\theta \sim IG(\alpha_*,\beta_*)$.

2.4 *Estimation*

For our application, we will partition the data such that the first n_0 complex-valued measurements which are different from the rest, are used as calibration measurements, although these can be a similar separate data set. These will be used to objectively assess the hyperparameters of the prior distributions which will then be combined with the steady-state signal to form an enhanced posterior signal. The average magnitude of the complex-valued calibration data $x_R + i\,x_I$ (where $i = \sqrt{-1}$) is computed to obtain the prior magnitude mean

$\rho_0 = \sqrt{\bar{x}_R^2 + \bar{x}_I^2}$. The hyperparameter $\gamma = n_0$ is assessed to be the number of calibration measurements. The four-quadrant arctangent of the averaged complex-valued calibration data is computed to obtain the prior phase mean $\theta_0 = \arctan_4(\bar{x}_R/\bar{x}_I)$. Lastly, the prior distribution quantity $\sigma_0^2 = (s_R^2 + s_I^2)/2$ is computed as the average variance of the real and imaginary parts of the calibration measurements. The hyperparameters of shape and scale are assessed to be $\alpha = n_0 - 1$ and $\beta = (n_0 - 1)\sigma^2$ respectively. This Bayesian model also supports the ability to assess hyperparameters from non-previous data, such as expert opinion.

When only one value is needed, such as the mode, we can use the iterated conditional modes (ICM) algorithm to obtain a maximum *a posteriori* (MAP) estimate (Lindley and Smith, 1972; O'Hagan, 2003). The modes of the conditional distributions in Equations 13-15 are given by

$$\hat{\rho} = \frac{C + \sqrt{C^2 + 8B(A-1)}}{4B}, \tag{16}$$

where $A = 2$, $B = (\gamma + 1)/(2\sigma^2)$, and $C = \left[\rho_0\gamma\cos(\theta - \theta_0) + r\cos(\phi - \theta)\right]/\sigma^2$,

$$\hat{\theta} = \arctan\left(\frac{b}{a}\right), \tag{17}$$

where $a = \rho_0\gamma\cos(\theta_0) + r\cos(\phi)$, $b = \rho_0\gamma\sin(\theta_0) + r\sin(\phi)$, and

$$\hat{\sigma}^2 = \frac{\beta_*}{\alpha_* + 1}, \tag{18}$$

where $\beta_* = \left[(\gamma+1)\rho^2 - 2\rho(\rho_0\gamma\cos(\theta - \theta_0) + r\cos(\phi - \theta)) + (\gamma\rho_0^2 + r^2 + 2\beta)\right]/2$ and $\alpha_* = \alpha + 2$.

The ICM algorithm starts with an initial value for the parameters $\hat{\rho}$ and $\hat{\sigma}^2$. Based on these values, an estimation of the parameter $\hat{\rho}$ is made using Equation 16. Each iteration of the algorithm will continue to obtain the MAP estimate for each of these parameters based on the most recent value of the other, using Equations 16-18. This is performed for each of the parameters until convergence is reached, as shown in Algorithm 1. In this work, this could be performed in as few as $L = 3$ iterations but is generally allowed up to $L = 10$

at a negligible computational cost. If there exists a unique global maxima, as is the case with each of our unimodal posterior conditional distributions, then the iterative parameter estimates will converge to this maximum. Note that since Equation 17 does not depend on ρ or σ, the mode of the phase $\hat{\theta}$ can be immediately estimated without the ICM algorithm.

Algorithm 1 ICM Algorithm for L iterations

```
$\hat{\theta} \leftarrow f(a, b)$                              ▷ Equation 17
$\hat{\rho}_{(1)} \leftarrow 1$                                ▷ Initialize guess
$\hat{\sigma^2}_{(1)} \leftarrow 1$                            ▷ Initialize guess
for $l = 2 : L$ do
    $\hat{\rho}_{(l)} \leftarrow f(\hat{\theta}, \hat{\sigma^2}_{(l-1)})$      ▷ Equation 16
    $\hat{\sigma^2}_{(l)} \leftarrow f(\hat{\rho}_{(l)}, \hat{\theta})$        ▷ Equation 18
end for
$\hat{\rho} \leftarrow \hat{\rho}_{(L)}$                       ▷ Final parameter estimate
$\hat{\sigma^2} \leftarrow \hat{\sigma^2}_{(L)}$               ▷ Final parameter estimate
```

Since we have the posterior conditional distributions in Equations 13-15, we could also perform a Gibbs sampling to obtain an entire distribution and compute any desired quantity such as marginal posterior means (MPM) (Geman and Geman, 1984; Gelfand and Smith, 1990). An initial estimate for the parameters ρ, θ, and σ^2 is made. Following this, sequential random samples are collected from each of the posterior conditional distributions given by Equations 13-15 using the initial estimates. This step is repeated for L iterations, each using the latest sample for each parameter. The first B samples are often burned, leaving a final set of $L - B$ samples for each parameter. The samples are then averaged for each parameter, resulting in MPM estimates. This process is outlined in Algorithm 2 below. Random samples from the MHN distribution for the magnitude ρ are generated using an acceptance-rejection method described by Algorithm 1 from Sun et al. (2023). Random samples from the von

Mises distribution for the phase θ are also generated from an acceptance-rejection method that employs the wrapped Cauchy distribution, as outlined in Section 4 from Best and Fisher (1979). Lastly, random samples from the inverse gamma distribution for the variance σ^2 are generated directly using MATLAB's built in `gamrnd()` function.

Algorithm 2 Gibbs Sampler for L iterations with $B < L$ burned samples

```
$\rho_{(1)} \leftarrow 1$                                              ▷ Initialize guess
$\theta_{(1)} \leftarrow 1$                                            ▷ Initialize guess
$\sigma^2_{(1)} \leftarrow 1$                                          ▷ Initialize guess
for $l = 2 : L$ do
    $\rho_{(l)} \leftarrow f(\theta_{(l-1)}, \sigma^2_{(l-1)})$        ▷ Equation 13
    $\theta_{(l)} \leftarrow f(\rho_{(l-1)}, \sigma^2_{(l-1)})$        ▷ Equation 14
    $\sigma^2_{(l)} \leftarrow f(\rho_{(l-1)}, \theta_{(l-1)})$        ▷ Equation 15
end for
$\hat{\rho} \leftarrow \bar{\rho}_{(B:L)}$                             ▷ Final parameter estimate
$\hat{\theta} \leftarrow \bar{\theta}_{(B:L)}$                         ▷ Final parameter estimate
$\hat{\sigma^2} \leftarrow \bar{\sigma^2}_{(B:L)}$                     ▷ Final parameter estimate
```

3. Illustrative Example

To demonstrate the effectiveness of the described method in enhancing complex-valued signals, a simple simulated experiment will be performed. Consider a single complex-valued signal that is measured over 100 time points where the first three measurements are of higher signal magnitude than the remaining 97 (which are at a steady state with 1/3 of the intensity of the first measurement). The magnitude and phase of this original data set are shown in black in Figure 1. Prior estimates for the magnitude and phase were calculated using the method described in Section 2.4, with the first three measurements serving as calibration data. The remaining 97 measurements serve individually as the likelihood. The ICM algorithm and Gibbs sampling technique were then both implemented, as described in Algorithms 1 and 2, to obtain the MAP and MPM estimates respectively. The ICM algorithm was run using $L = 15$ iterations and took about 0.02 seconds total. Generally, convergence was reached after only three iterations. There were 5,000 Gibbs samples including a 500 sample burn-in phase, resulting in 4500 samples for MPM estimation at each time point. This took a total of 2 seconds to simulate using MATLAB's parallel computing toolbox (it took 8 seconds to run in serial). The MAP and MPM estimates are shown in blue and red in Figure 1, respectively. Qualitative diagnostics were performed to verify proper mixing and the stochastic convergence of observations. Both posterior estimation methods similarly improve the original data with a noticeable suppression of noise. Since the Gibbs samples have the added benefit of uncertainty quantification, 95% confidence intervals are shown as well. The original data had an SNR of 5.3 while the MAP and MPM estimates had improved SNRs of 45.1 and 46.7, respectively. This is an improvement by a factor of about 9 for both methods.

[Figure 1 about here.]

4. FMRI Application

FMRI is a commonly used non-invasive imaging technique that allows physicians and scientists to observe the functionality of organs such as the human brain. This is done by exciting hydrogen nuclei in the various water molecules that make up the different tissues of the organ with a radio frequency (RF) pulse, then measuring a resulting net change in magnetization as determined by an induced current in a loop of wire that surrounds the patient. The intensity of the net magnetization in different voxels of the region of interest (ROI) is associated with complex-valued spatial frequency coefficients that fill k-space; a high order approximation of the Fourier transform of the image of the organ. The k-space is then inverse discrete Fourier transformed (IDFT) to reconstruct an image of the slice that is being observed. In fMRI experiments, this process is repeated many times; each volume image taking about 1 second to collect. A series of "task" and "non-task" images are collected where the patient is instructed to perform some task, such as right-hand finger tapping. This results in an expected increase of signal in the "task" images in certain regions of the brain, in this case-the *left* motor cortex.

It is well known in fMRI studies that the first three or so images in a time series have much higher signal than the remainder of the time series. Assuming the experiment starts in thermal equilibrium, the net magnetization is entirely in the longitudinal direction, so $M_Z(0) = M_0$ and $M_{XY}(0) = 0$. After the first pulse RF_1 at some flip angle α, the longitudinal and transverse magnetization will become $M_Z(RF_1) = M_0 \cos(\alpha)$ and $M_{XY}(RF_1) = M_0 \sin(\alpha)$. Due to the fact that $TR \approx T_1$ for fMRI experiments, the longitudinal component of the magnetization, M_Z, will not yet be fully recovered by the time of the second pulse RF_2. After a sufficient number of RF pulses (generally two or three), the system will reach a steady state where each RF pulse beyond this point results in the same magnetization value for the longitudinal direction, called M_{SS}. Since the first three reconstructed images do not match the observed signal from the remainder of the time series, they are often discarded, and only the steady-state images are analyzed.

When Bayesian analysis of fMRI data is done on image-space data, voxels may be spatially correlated, quite often due to image preprocessing, demanding the use of a spatial model (Penny et al., 2005; Wang et al., 2024; Yu et al., 2023). It is well understood, however, that the Fourier transform of correlated voxels results in uncorrelated spatial frequency coefficients (Kornak et al., 2024). Thus, we chose to employ our Bayesian method on the uncorrelated k-space data prior to IFT since the spatial frequency coefficients can be treated independently of each other. Since the analog-to-digital converters (ADCs) collect the original k-space measurements independently, it is understood that the real and imaginary parts of a given k-space measurement (k_R, k_I) are independent and identically distributed (iid) normally for each spatial frequency location. The transformation $k_R = r_k \cos(\phi_k)$ and $k_I = r_k \sin(\phi_k)$ allows us to work with the k-space measurements in polar space.This experimental setup precisely matches the theory established in Section 2.

Previous work on Bayesian image analysis in Fourier space (BIFS) has been done on polar coordinates (Kornak et al., 2024; Bakas et al., 2025). The BIFS method operates in a Fourier space that is constructed from the Fourier transform of a noisy real-valued image after the phase has been discarded, resulting in a Hermitian symmetric Fourier space. An MCMC Bayesian method to enhance each of the the complex-valued spatial frequency coefficients is conducted. The result is then inverse Fourier transformed back into a de-noised image. In fMRI the complex-valued spatial frequency coefficients in k-space are measured directly and then inverse Fourier transformed into image space. The method outlined in Section 2 as applied to this problem can be seen as an extension to BIFS that is applied directly to a measured Fourier space (k-space) and makes use of mathematically correct conjugate prior distributions which leads to simpler estimation. All distributions and parameters in this section are analyzed in k-space unless stated otherwise.

4.1 *Experimental Data Description*

The experimental data used in this section is from a block-design unilateral right-hand finger tapping experiment collected on a 3.0-Tesla General Electric Signa LX MRI scanner. Brain image data was collected using a body coil that resulted in a low SNR. There were seven excited axial slices $n_s = 7$ of 2.5 mm thickness with an array size of 128×128 with a field-of-view FOV = 24 cm, echo time TE = 50 ms, effective echo spacing EESP = 0.832 ms, and repetition time TR = 1 s. For this paper, we look at the time series for only the sixth slice of the seven collected. The experiment included 16 initial seconds of rest followed by 19 epochs each consisting of 16 seconds of task followed by 16 seconds of rest, resulting in 624 total images $n_t = 624$. It is often observed that the magnetic fields in an fMRI experiment will induce a drift in the phase over time which we corrected before reconstruction to give us a stable phase through time (Sakitis and Rowe, 2025). First, the angular phase temporal mean of each k-space element's time-series is calculated and angularly subtracted. A local second order polynomial was spatially fit to the resultant difference of the k-space element phase time-series. Then the spatially fitted phase is angularly subtracted from the original phase, the residual phase was unwrapped and linearly detrended, then the angular phase temporal mean was angularly added back, producing a linearly stable phase over time for each spatial frequency. Figure 2 shows the magnitude and phase of the first four k-space arrays and corresponding reconstructed images in the time series. The remainder of the time series appears similarly to TR 4.

[Figure 2 about here.]

4.2 *Estimation*

The first three k-space arrays have decreasing intensity and are not consistent with the remaining arrays. In common practice, these measurements would be omitted prior to computing activation. Instead, we will use the first $n_0 = 3$ k-space arrays as calibration data, or "prior" information. These will be used to assess the hyperparameters of the prior distributions that will be combined with the steady-state k-space observations to form enhanced posterior reconstructed images. The remaining 621 k-space arrays will be considered as the "observed" data. The estimation method will be similar to that described in Section 2.4 and exemplified in Section 3, but applied to each k-space element through time individually ($128 \times 128 \times 621 = 10,174,464$ complex-valued data points in total). At each k-space spatial frequency, the magnitude of the averaged prior k-space measurements is computed for the prior mean $\rho_0 = \sqrt{\bar{k}_R^2 + \bar{k}_I^2}$. The hyperparameter $\gamma = n_0$ is assessed to be the number of calibration arrays. We set $\gamma = n_0 = 3$ due to the previous theoretical description on magnetic saturation. The four-quadrant arctangent of the averaged prior k-space measurements is computed for the prior mean $\theta_0 = \arctan_4(\bar{k}_R/\bar{k}_I)$. Lastly, the prior distribution quantity $\sigma_0^2 = (s_R^2 + s_I^2)/2$ is computed as the average of the variance of the real and imaginary parts of the prior k-space measurements. The prior hyperparameters are assessed to be $\alpha = n_0 - 1 = 2$ and $\beta = (n_0 - 1)\sigma^2 = 2\sigma^2$.

The magnitude and phase of each k-space spatial frequency location is individually estimated. We implement both the ICM algorithm and Gibbs sampling techniques as described by Algorithms 1 and 2 to obtain posterior estimates. Similarly to Section 3, the ICM algorithm was run with $L = 15$ iterations at each time point for each k-space element, but in practice it took as few as 3 iterations to reach convergence. For the experimental data, there were 5,000 Gibbs samples generated including a 500-sample burn-in phase, resulting in 4500 samples for MPM estimation at each time point for each k-space element. This was done using MATLAB's parallel computing toolbox to decrease the necessary compute time. The experimental ICM data takes only a few seconds to run on a single computing core, while the Gibbs samples took several days in parallel across 20 computing cores. The precomputed prior k-space arrays and corresponding reconstructed images as well as the likelihood and posterior estimates for the final TR in steady state are presented in Figure 3. The second column, "Observed" is representative of the latter 621 images in the time series. Both Bayesian methods enhance image contrast and decrease noise when compared to the observed data. Increased image contrast can lead to improved image segmentation, feature extraction, and classification (Zhou et al., 2019).

[Figure 3 about here.]

4.3 *Results*

Task-based fMRI for an individual voxel's magnitude time series y_t can be expressed as the linear equation

$$y_t = \beta_0 + \beta_1 x_t + \varepsilon_t. \tag{19}$$

The additive noise ε_t is Ricean distributed with variance σ^2. Here, $\beta_0 \in \mathbf{R}^+$ is the baseline signal which determines the signal-to-noise ratio $SNR = \beta_0/\sigma$, and $\beta_1 \in \mathbf{R}$ is the task-related signal increase which determines the contrast-to-noise ratio $CNR = \beta_1/\sigma$. The design vector $x_t \in \{0, 1\}^{n_t}$ has length equal to the number of reconstructed images in the time series, n_t. In x, indices corresponding to a non-task image have an element of 0, while indices corresponding to a task-active image have an element of 1.

The SNR for the original data, the MAP estimates, and the MPM estimates are shown in Figure 4 (top row). Note that the upper scaling for the color bar is increased from 5 to 30 for the Bayesian posterior estimates. Both Bayesian methods similarly improved the SNR when compared to the original data. Slight timing differences when measuring spatial frequency coefficients in k-space result in a Nyquist ghost above and below the brain, this is apparent in the SNR of the Bayesian methods in the experimental data. The CNR is an indication of where the increase in task activation-related signal is measured. The CNR calculated from the original data and the two Bayesian methods is shown in Figure 4 (second row) with a fixed color bar. Both posterior estimations accurately capture the task activation in the left motor cortex associated with the right hand finger tapping, as indicated by the yellow region. When comparing the posterior estimated data to the original data, it is clear that we have significantly decreased the effect of noise on the data, while still maintaining fidelity to detect task-related activation. Having improved contrast in images, like those produced by the MAP and MPM estimation methods, will allow for better image registration when correcting for motion as well as assist image segmentation when labeling regions of interest. We recommend the use of the ICM algorithm to generate MAP estimates for this application. The temporal cost is minimal with vastly improved signal quality when compared to the original data. This approach preserves activation while decreasing noise and increasing SNR.

When a voxel is active as a result of the BOLD response, the magnitude can change, the phase can change, or a combination of both can occur (Rowe, 2005). This model supports a complex-valued task activation related BOLD signal change. A simple t test is conducted on the experimental images at rest compared to the images collected while the task was active. The results presented in the bottom two rows of Figure4 highlight detected activation in the left motor cortex (the region where task activation is expected for the right-hand finger tapping experiment). It is clear that voxels in this region exhibit both an increase in magnitude as well as an associated change in phase that correlate to task performance. Further, both estimation methods preserve the ability to detect task in the posterior enhanced data.

[Figure 4 about here.]

5. Discussion

Systems that receive complex-valued signals can often suffer from signal loss and degradation over time. Here, we implement a Bayesian approach to enhance the noisy signal using only a small number of prior strong measurements. This process is demonstrated on simple simulated data in Section 3. The results of the experimental fMRI studies in Section 4 demonstrate that the model can increase the SNR of the original data, leading to higher contrast reconstructed images. A description of simulated fMRI data where the model was tested before validating on experimental data can be found in Web Appendix A of the accompanying supplementary materials.

We used full posterior distributions for the estimation of parameters magnitude ρ, phase θ, and variance σ^2. This includes, to our knowledge, the first application of the recently described MHN distribution (Sun et al., 2023). This allowed us to apply both the ICM algorithm and a Gibbs sampling technique to our model. The signal amplification for the experimental data was done using the ICM algorithm with $L = 15$ iterations and Gibbs sampling with $5,000$ samples; both methods were applied at each k-space element at each time point. Due to the significant difference in computational expense with minimal effect on results, we recommend the use of the ICM algorithm to obtain MAP estimates. The Gibbs sampler has the added benefit of quantifying uncertainty since it generates distributions of estimates as compared to a point estimate from the ICM algorithm, so if computational time is not a concern Gibbs samples may be worth collecting.

The ability to detect task in the MAP and MPM reconstructed images is not hindered by the use of rest images to form the prior. The MAP and MPM reconstructed images have an increased SNR and improved contrast from the original data, allowing for better image registration and segmentation. This will help physicians correct for motion artifacts and to more easily segment regions of interest within the brain.

ACKNOWLEDGEMENTS

The authors would like to thank the Northwestern Mutual Data Science Institute for contributing funding towards this research.

REFERENCES

Bakas, K., Kornak, J., and Ombao, H. (2025). An MCMC Approach to Bayesian Image Analysis in Fourier Space. *Data Science in Science* **4,** 2452603.

Best, D. J. and Fisher, N. I. (1979). Efficient simulation of the von Mises distribution. *Journal of the Royal Statistical Society Series C: Applied Statistics* **28,** 152–157.

Bodenschatz, J. C. and Rowe, D. B. (2025). Simulation and Harmonic Analysis of k-Space Readout (SHAKER).

den Dekker, A. J. and Sijbers, J. (2005). Implications of the Rician distribution for fMRI generalized likelihood ratio tests. *Magnetic Resonance Imaging* **23,** 953–959.

Fox, C. (1928). The asymptotic expansion of generalized hypergeometric functions. *Proceedings of the London Mathematical Society* **s2-27,** 389–400.

Gelfand, A. E. and Smith, A. F. M. (1990). Sampling-based approaches to calculating marginal densities. *Journal of the American Statistical Association* **85,** 398–409.

Geman, S. and Geman, D. (1984). Stochastic relaxation, Gibbs distributions, and the Bayesian restoration of images. *IEEE Transactions on Pattern Analysis and Machine Intelligence* **PAMI-6,** 721–741.

Gudbjartsson, H. and Patz, S. (1995). The Rician distribution of noisy MRI data. *Magnetic Resonance in Medicine* **34,** 910–914.

Harris, J. J., Reynell, C., and Attwell, D. (2011). The physiology of developmental changes in BOLD functional imaging signals. *Developmental Cognitive Neuroscience* **1,** 199–216.

Kornak, J., Young, K., and Friedman, E. (2024). Bayesian image analysis in Fourier space.

Lathi, B. (1983). *Modern Digital and Analog Communication.* Oxford University Press.

Lindley, D. V. and Smith, A. F. M. (1972). Bayes estimates for the linear model. *Journal of the Royal Statistical Society. Series B (Methodological)* **34,** 1–41.

Mullinger, K., Mayhew, S., Bagshaw, A., Bowtell, R., and Francis, S. (2014). Evidence that the negative BOLD response is neuronal in origin: A simultaneous EEG–BOLD–CBF study in humans. *NeuroImage* **94,** 263–274.

Ogawa, S., Lee, T. M., Kay, A. R., and Tank, D. W. (1990). Brain magnetic resonance imaging with contrast dependent on blood oxygenation. *Proceedings of the National Acadamy of Sciences U. S. A.* **87,** 9868–9872.

O'Hagan, A. (2003). *Kendall's advanced theory of statistic 2B.* Kendall's advanced theory of statistics. Wiley-Blackwell, Hoboken, NJ.

Penny, W. D., Trujillo-Barreto, N. J., and Friston, K. J. (2005). Bayesian fMRI time series analysis with spatial priors. *NeuroImage* **24,** 350–362.

Rayleigh, L. (1880). Xii. on the resultant of a large number of vibrations of the same pitch and of arbitrary phase. *The London, Edinburgh, and Dublin Philosophical Magazine and Journal of Science* **10,** 73–78.

Rice, S. O. (1944). Mathematical analysis of random noise. *Bell System Technical Journal* **23,** 282–332.

Rowe, D. B. (2005). Modeling both magnitude and phase of complex fMRI data. *NeuroImage* **25,** 1310–24.

Rowe, D. B. (2023). Statistics of intrinsic FMRI data. *Proceedings of the Joint Statistical Meeting* .

Rowe, D. B. and Bodenschatz, J. C. (2025). Distributionally accurate FMRI phase activation. *Proceedings of the Joint Statistical Meeting* .

Sakitis, C. J. and Rowe, D. B. (2025). Bayesian merged utilization of GRAPPA and SENSE (BMUGS) for in-plane accelerated reconstruction increases fMRI detection power. *Magnetic Resonance Imaging* **115,** 110252.

Shmuel, A. and Leopold, D. A. (2008). Neuronal correlates of spontaneous fluctuations in fMRI signals in monkey visual cortex: Implications for functional connectivity at rest. *Human Brain Mapping* **29,** 751–761.

Sun, J., Kong, M., and Pal, S. (2023). The Modified-Half-Normal distribution: Properties and an efficient sampling scheme. *Communications in Statistics - Theory and Methods* **52,** 1591–1613.

Von Mises, R. (1918). Uber die 'ganzzahligkeit' der atomgewicht und verwandte fragen. *Physikalische Zeitschrift* **19,** 490–500.

Wang, Z., Rowe, D. B., Li, X., and Brown, D. A. (2024). A fully Bayesian approach for comprehensive mapping of magnitude and phase brain activation in complex-valued fMRI data. *Magnetic Resonance Imaging* **109,** 271–285.

Wright, E. M. (1935). The asymptotic expansion of the generalized hypergeometric function. *Journal of the London Mathematical Society* **s1-10,** 286–293.

Yu, C., Prado, R., Ombao, H., and Rowe, D. (2023). Bayesian spatiotemporal modeling on complex-valued fMRI signals via kernel convolutions. *Biometrics* **79,** 616–628.

Zhou, Y., Shi, C., Lai, B., and Jimenez, G. (2019). Contrast enhancement of medical images using a new version of the world cup optimization algorithm. *Quantitative Imaging in Medicine and Surgery* **9,**.

SUPPLEMENTARY MATERIAL

Web Appendix A, referenced in Section 5 is available with this paper at the Biometrics website on xxxxxOUP sitexxxxx. The software used to simulate fMRI data can be found at `https://github.com/bodensjc/SHAKER` (Bodenschatz and Rowe, 2025).

Received November 2025. *Revised Month* YYYY. *Accepted Month* YYYY.

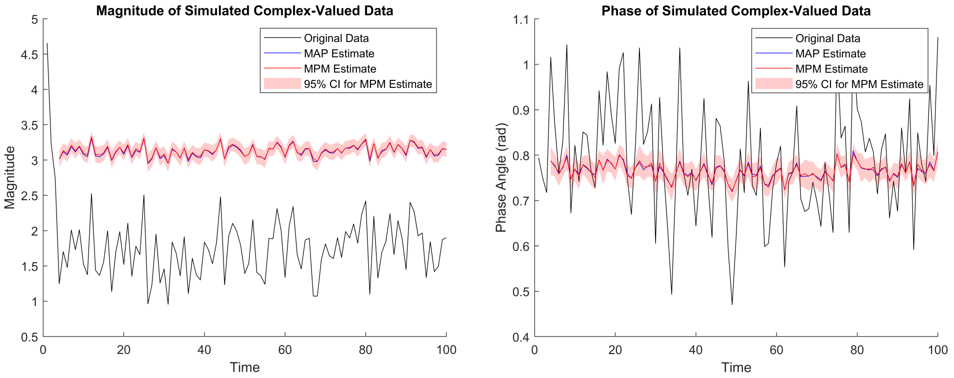

Figure 1: Magnitude and phase of the simulated complex-valued data. The original data has a much lower SNR than the improved MAP and MPM estimates.

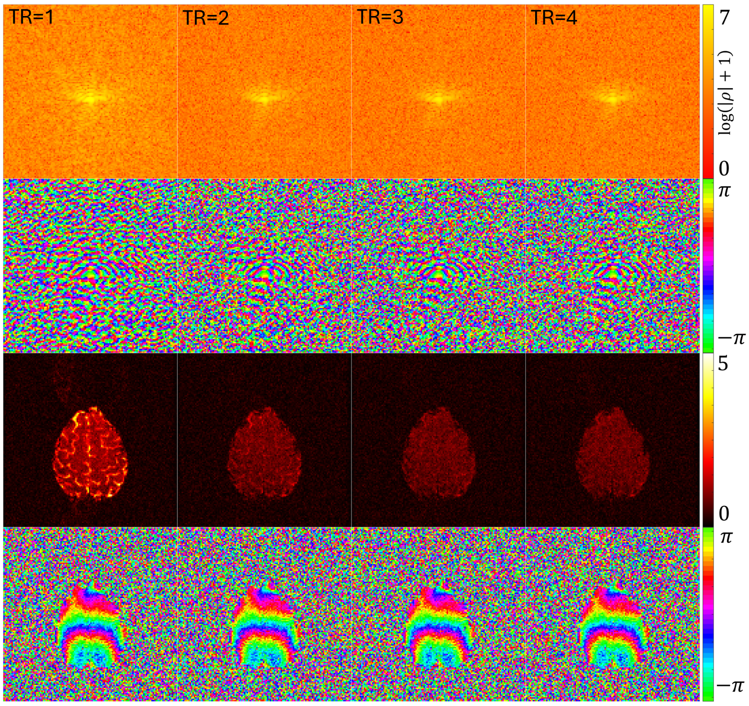

Figure 2: The magnitude and phase of both k-space and reconstructed images for the first four TRs in the experimental time series. The color bar is consistent across TRs so the signal degradation is clear.

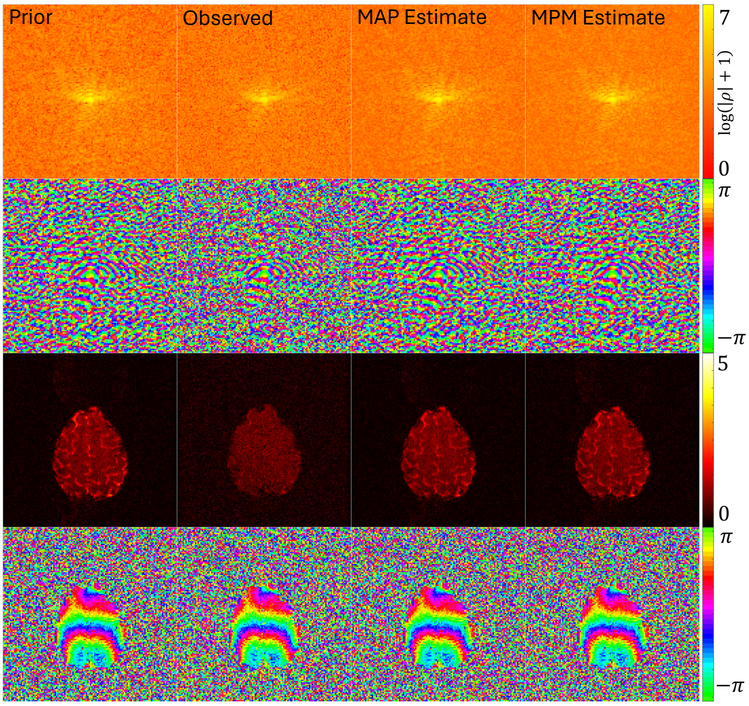

Figure 3: The magnitude and phase of both k-space and reconstructed images for the prior distribution, likelihood (measured data at $TR = 624$), and posterior estimates of the experimental data. Both Bayesian methods enhance image contrast when compared to the observed data.

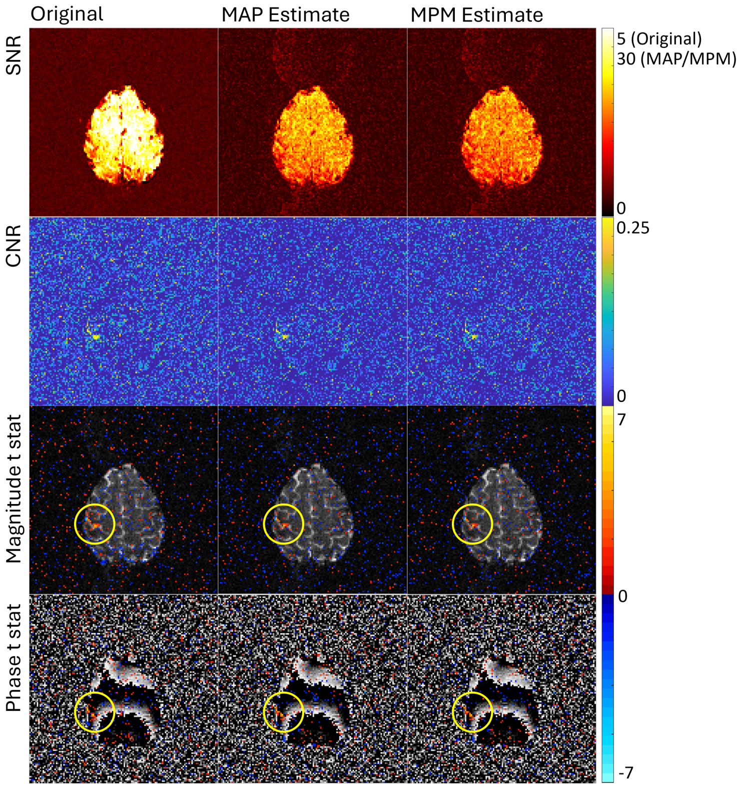

Figure 4: The SNR for the original data, MAP and MPM estimates (first row). Note the differing color bar scales- the MAP and MPM estimates have significantly increased SNR. The CNR for the original data, MAP and MPM estimates (second row). Both posterior estimates have similar CNR to the original data, indicating no loss in ability to detect task related activation. T statistics for activation related changes in magnitude (third row) and phase (fourth row) signals for the original data, MAP and MPM estimates. The highlighted region, the left motor cortex, corresponds to the expected area of activation when a right-hand finger tapping experiment is conducted.

Biometrics VV, 1–2
Month YYYY

DOI: DOI HERE

Supplementary Material for A Bayesian Model to Enhance Complex-Valued Measurements Applied to Functional Magnetic Resonance Imaging

by John C. Bodenschatz and Daniel B. Rowe

John Bodenschatz*, **and Daniel Rowe****

Department of Mathematical and Statistical Sciences, Marquette University, Milwaukee, WI, U.S.A.

**email:* john.bodenschatz@marquette.edu

***email:* daniel.rowe@marquette.edu

Summary: This paper contains supplemental material to the manuscript titled *A Bayesian Model to Enhance Complex-Valued Measurements Applied to Functional Magnetic Resonance Imaging* by John C. Bodenschatz and Daniel B. Rowe. The simulated fMRI study referenced in the main article is presented here, with corresponding results. The proposed Bayesian method enhances the low signal, noisy simulated data. Enhanced reconstructed images are generated, with task activation detection preserved. These methods are validated in the main article on experimental fMRI data.

Key words: Bayesian; Complex-Valued; FMRI; K-space.

This paper has been submitted for consideration for publication in *Biometrics*

1. Web Appendix A

The following fMRI time series data was simulated using SHAKER v1.1 (Bodenschatz and Rowe, 2025). The simulated time series is of slice 83 from a size 128×128 phantom in the Axial plane. The MRI parameters were set to be the following: Acceleration Factor = 1, Field Strength = 3 T, TE = 50 ms, TR = 1000 ms, Flip Angle = 90 deg, EESP = 0.832 ms, and Number of Coils = 1. The data was simulated with the Gradient Echo signal equation using a Cartesian k-space trajectory. The experimental design involved an initial 16 rest images followed by 19 epochs, each consisting of 16 task images followed by 16 rest images, for a total of 624 images. In voxels designed to be active, the SNR was set to 5 and the CNR was set to 0.25. There were 3 degrees of phase added to the task-related activation. Images were reconstructed using the inverse Fourier transform. These options were chosen to maintain consistency with the experimental data. Web Figure 1 shows the magnitude and phase of the first four k-space arrays and corresponding reconstructed images in the time series. The remainder of the time series appears similar to TR 4.

[Web Figure 1 about here.]

The posterior data is estimated in a similar fashion to the experimental data as described in Section 4.2 from the main article. The only difference for the simulated data being that there were 200 Gibbs samples generated including a 50-sample burn-in phase, resulting in 150 samples for MPM estimation at each time point for each k-space element (rather than the 4500 samples for the experimental data). The precomputed prior k-space arrays and corresponding reconstructed images as well as the likelihood and posterior estimates for the final TR in steady state are presented in Figure 2. The second column, "Observed" is representative of the latter 621 images in the time series. Both Bayesian methods enhance image contrast and decrease noise when compared to the observed data.

[Web Figure 2 about here.]

The SNR for the original data, the MAP estimates, and the MPM estimates are shown in Web Figure 3 (top row). Note that the upper scaling for the color bar is increased from 5 to 30 for the Bayesian posterior estimates. Both Bayesian methods similarly improved the SNR when compared to the original data. The CNR calculated from the original data and the two Bayesian methods is shown in Web Figure 3 (second row) with a fixed color bar. Both posterior estimations accurately capture the task activation in the left motor cortex associated with the right hand finger tapping, as indicated by the yellow region in the bottom two rows of Web Figure 3.

[Web Figure 3 about here.]

ACKNOWLEDGEMENTS

The authors would like to thank the Northwestern Mutual Data Science Institute for contributing funding towards this research.

Received November 2025. *Revised Month* YYYY. *Accepted Month* YYYY.

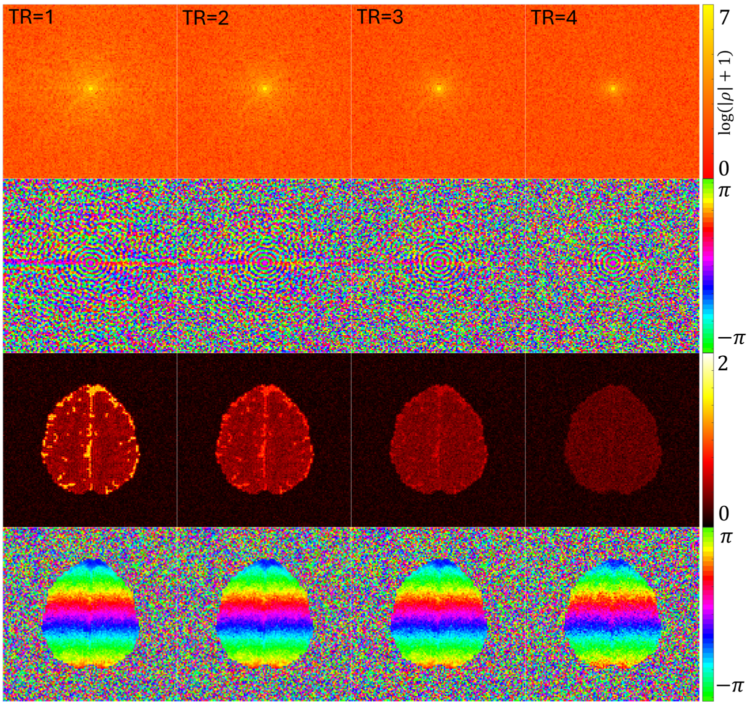

Figure 1: The magnitude and phase of both k-space and reconstructed images for the first four TRs in the experimental time series. The color bar is consistent across TRs so the signal degradation is clear.

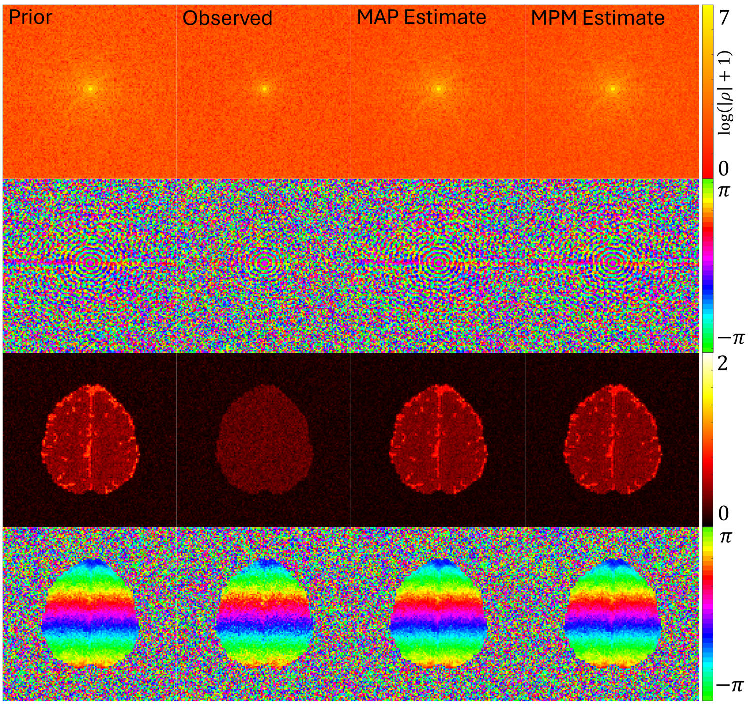

Figure 2: The magnitude and phase of both k-space and reconstructed images for the prior distribution, likelihood (simulated data at $TR = 624$), and posterior estimates of the simulated data. Both Bayesian methods enhance image contrast when compared to the observed data.

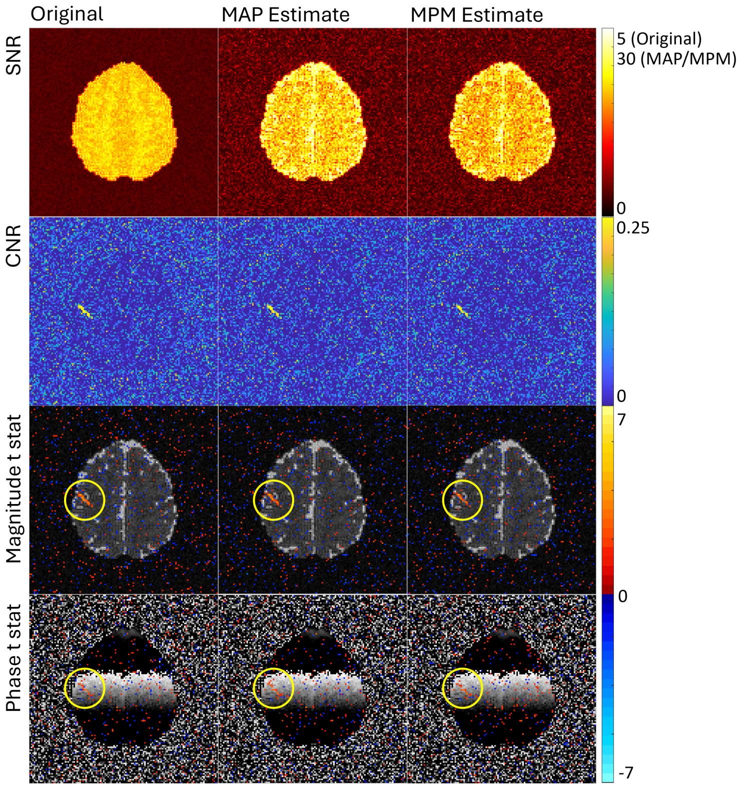

Figure 3: The SNR for the original data, MAP and MPM estimates (first row). Note the differing color bar scales- the MAP and MPM estimates have significantly increased SNR. The CNR for the original data, MAP and MPM estimates (second row). Both posterior estimates have similar CNR to the original data, indicating no loss in ability to detect task related activation. T statistics for activation related changes in magnitude (third row) and phase (fourth row) signals for the original data, MAP and MPM estimates. The highlighted region, the left motor cortex, corresponds to the expected area of activation when a right-hand finger tapping experiment is conducted.